

## Three-dimensional surface motion maps estimated from combined interferometric synthetic aperture radar and GPS data

Sverrir Gudmundsson and Freysteinn Sigmundsson

Nordic Volcanological Institute, Reykjavik, Iceland

Jens Michael Carstensen

Institute for Mathematical Modeling, Technical University of Denmark, Lyngby, Denmark

Received 22 June 2000; revised 15 March 2002; accepted 20 March 2002; published 23 October 2002.

[1] We provide a technique to efficiently produce high-resolution three-dimensional surface motion maps by combining information about the motion of the Earth's surface from interferometric observations of synthetic aperture radar images and repeated Global Positioning System (GPS) geodetic measurements. Unwrapped interferograms, showing pixel-wise change in range from ground to satellite, and sparse values of three-dimensional movements are required as input. The problem of finding the full three-dimensional motion field is separated into two two-dimensional problems. Initially, the vertical component of the deformation field and its horizontal component in the look direction of the satellite are found. Later, the look direction component is resolved into north and east components. Initial values for the motion fields are assigned to each pixel of interferograms from interpolation of available GPS observations. These values are then updated and optimized by comparison with the interferograms and the GPS observations. An additional constraint is an assumption of a smoothly varying motion field. Markov random field-based regularization and simulated annealing algorithm are used for the optimization. The technique is applied to create surface motion maps for the Reykjanes Peninsula, SW Iceland. **INDEX TERMS:** 0933 Exploration Geophysics: Remote sensing; 0910 Exploration Geophysics: Data processing; 1206 Geodesy and Gravity: Crustal movements—interplate (8155); 8150 Tectonophysics: Evolution of the Earth: Plate boundary—general (3040); 8155 Tectonophysics: Evolution of the Earth: Plate motions—general; **KEYWORDS:** remote sensing, motion maps, deformation, data fusion, interferometry, GPS

**Citation:** Gudmundsson, S., F. Sigmundsson, and J. M. Carstensen, Three-dimensional surface motion maps estimated from combined interferometric synthetic aperture radar and GPS data, *J. Geophys. Res.*, 107(B10), 2250, doi:10.1029/2001JB000283, 2002.

### 1. Introduction

[2] Global Positioning System (GPS) geodetic measurements and interferometric analysis of synthetic aperture radar images (InSAR) provide two complementary views on the deformation of the Earth's surface [e.g., *Bock and Williams*, 1997]. Repeated GPS measurements provide point-wise information on three-dimensional movements at the occupied geodetic stations with subcentimeter accuracy [e.g., *Leick*, 1990]. The InSAR technique provides a map view of one component of the deformation field. SAR images acquired by radar satellites at different times can be combined into interferograms that reveal information about the change in range from ground to satellite (the slant range shift) with about 1 cm accuracy or less, expressed as interferometric fringes [e.g., *Massonnet and Feigl*, 1998]. Here we present a methodology for fusion of InSAR and GPS data, with three-dimensional (3-D) surface motion maps being the final product.

[3] Various image analysis methods can be used for such fusion. The methodology we present utilizes a Markov random field (MRF) based regularization and simulated annealing optimization [*Carstensen*, 1992; *Li*, 1995]. In MRF regularization, an optimal image is interpreted as a realization of a random variable, where the value of each pixel in the image grid is only dependent on its nearest neighbors. This provides a convenient way of modeling image texture and spatial correlation of image pixels. Furthermore, simulated annealing optimization of MRF regularization is a very suitable and effective method to use in image reconstruction.

[4] The method presented here can be used to construct 3-D motion maps of various types of surface movements. Such motion maps can be useful e.g., (1) to display data and provide a consistent view of 3-D motion fields, (2) to derive strain rate maps that can be used to study the buildup of crustal stresses related to future earthquakes, and (3) to infer volume of surface uplift/subsidence by integration of vertical deformation fields.

[5] The technique was applied by *Gudmundsson et al.* [2002b] to infer ice flow at the 1996 Gjalp eruption site in

Vatnajökull ice cap, Iceland, and to infer subglacial melting rates (volume changes) due to the cooling Gjalp volcano. There, integrated uplift was a key parameter to calculate the subglacial melting. Here the results of applying the method to infer crustal deformation on the Reykjanes Peninsula from InSAR and GPS observations from SW Iceland are presented. Also, in this paper we use synthetic motion of ice flow, created by an ice flow model, to obtain an estimate of errors and evaluate the technique we present.

## 2. Observations

### 2.1. Reykjanes Peninsula, SW of Iceland

[6] As a test area for our procedure we use the Reykjanes Peninsula, an obliquely spreading subaerial portion of the Mid-Atlantic Ridge in SW Iceland (Figure 1). A relatively dense GPS network has been measured in the area, and InSAR studies have been conducted there as well. The combination process presented in this paper requires InSAR interferograms in unwrapped format as an input. Four unwrapped interferograms from the Reykjanes Peninsula were available for this study (Figure 2 and Table 1), acquired from descending satellite passes. They are unwrapped versions of the interferograms used by *Vadon and Sigmundsson* [1997], in addition to one new interferogram (Figure 2c) formed in the same way as the others with the Centre National d'Etudes Spatiales developed DIAPASON software. Topographical effects have been eliminated by using a digital elevation model, and known orbital effects have also been removed. The wrapped interferograms were prefiltered with a vectorized filtering algorithm [*Gudmundsson*, 2000, p. 14; *Gudmundsson et al.*, 2002a], and unwrapped by a Markov random field (MRF) based unwrapping process [*Gudmundsson*, 2000, pp. 37–50; *Gudmundsson et al.*, 2002a]. The interferograms cover different elapsed time intervals within the 1992–1996 period. Pixel resolution in the nonfiltered interferograms is  $1/600^\circ$  in longitude and  $1/1200^\circ$  in latitude, or approximately  $93 \times 82$  m area. The interferograms may include residual topographical and orbital errors, as well as noise of atmospheric or ionospheric origin [e.g., *Massonnet and Feigl*, 1995; *Williams et al.*, 1998], and some noise due to coherence degradation [e.g., *Zebker and Villasenor*, 1992].

[7] GPS measurements were conducted at 38 points at the Reykjanes Peninsula in 1993 and repeated in 1998. Description of the GPS data processing is given by *Hreinsdóttir* [1999] and *Hreinsdóttir et al.* [2001]. The locations of the GPS points are shown in Figure 3, along with average horizontal and vertical velocities inferred from GPS for the 1993–1998 period. A velocity of 8.3 mm/yr in the N79°W direction has been assumed for the Reykjavik GPS station (ARNA station of *Hreinsdóttir* [1999, p.72]), but this station was used as a reference station when processing the GPS data and its position was held fixed in the data processing. Precise orbit information given in the ITRF91 reference frame [*Boucher and Altamimi*, 1996], were used to calculate site coordinates relative to the reference station for the 1993 GPS data, and the ITRF96 reference frame [*Rothacher et al.*, 1998] was then used for the 1998 data. The GPS measured velocities in Figure 3 and corresponding uncertainties are tabulated

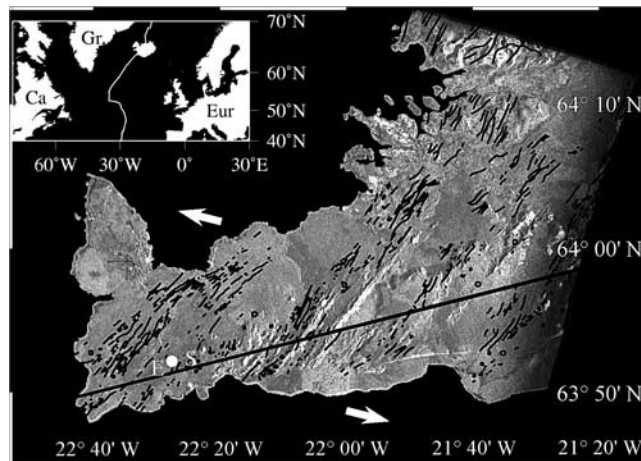


**Figure 1.** Reykjanes Peninsula, SW Iceland. The image shows the locations of faults and eruptive fissures as black lines, imprinted on a SAR amplitude image. The thick line indicates the approximate location of central axis of the plate boundary as inferred from seismicity [*Einarsson*, 1991]. E and S denote the Eldvörp and Svartsengi geothermal areas, and white dot marks a center of subsidence inferred from geodetic data. The two arrows indicate the plate motions, which is 19 mm/yr in the direction N103°E (full spreading) according to the NUVEL-1A plate model [*DeMets et al.*, 1994]. Modified from *Vadon and Sigmundsson* [1997].

by *Hreinsdóttir et al.* [2001, p. 13,806]. The uncertainty values range from 0.7 to 4.2 mm/yr for the vertical components and from 0.5 to 1.1 mm/yr for the horizontal components, with mean values of  $\sim 2.4$  and  $\sim 0.6$  mm/yr, respectively. The observed vertical velocities exceed their uncertainty for 31 of the 38 GPS sites. Most of the GPS observed displacement rates show high spatial consistency (Figure 3) and we have observed a good consistency in general between the InSAR and GPS data sets from the Reykjanes Peninsula.

[8] The InSAR interferograms and the GPS measurements cover different elapsed time intervals, but crustal deformation at the Reykjanes Peninsula in the 1992–1998 period can be assumed to be mostly smooth. No large earthquakes have been recorded there during this period [*Hreinsdóttir*, 1999; *Vadon and Sigmundsson*, 1997]. The interferograms in Figure 2 suggest some time variability for some parts of the image areas. This time dependence has to be considered before the interferometric and GPS data can be combined since the observations cover somewhat different time intervals.

### 2.2. Synthetic Motion Maps of Ice Flow

[9] In addition to the interferograms from the Reykjanes Peninsula, a  $164 \times 164$  pixel synthetic interferogram and corresponding motion maps were created for experimental purpose (Figure 4). These were created by using a mass balance equation to describe surface ice flow at an axisymmetrical glacier cauldron [e.g., *Björnsson et al.*, 2001]. No noise was included, and motion maps were all known. Assuming GPS observations at selected points gives an

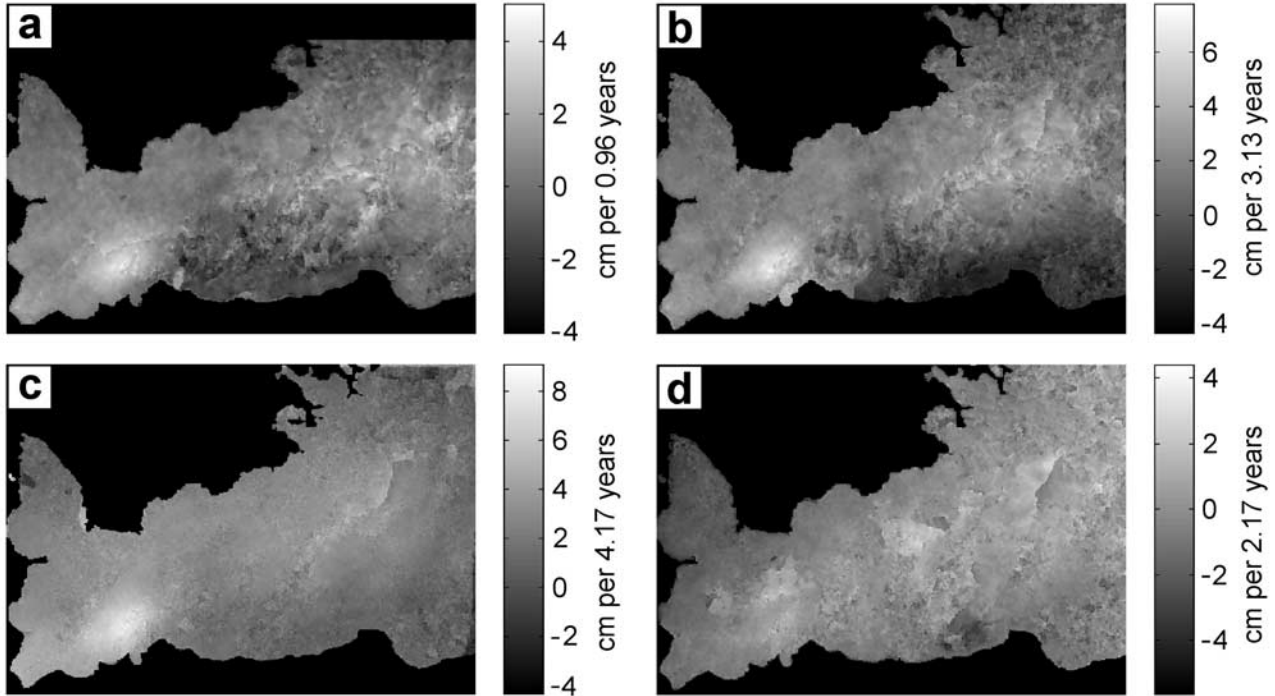


**Figure 2.** Unwrapped InSAR interferograms from the Reykjanes Peninsula, listed in Table 1. The interferograms have been prefiltered with  $3 \times 3$  pixels moving average window.

opportunity to test the procedure, and obtain an estimate of errors.

### 3. Description of the Problem

[10] An InSAR interferogram records the slant range shift as

$$V_{\text{SRS}_k} = -[V_{E_k}, V_{N_k}, V_{V_k}][u_E, u_N, u_V]^T, \quad \forall k, \quad (1)$$

where  $k$  is a pixel number,  $V_{E_k}$ ,  $V_{N_k}$ , and  $V_{V_k}$  are the east, north, and vertical components of deformation, respectively, and  $\mathbf{s} = [u_E, u_N, u_V]^T$  is a unit vector pointing from the ground toward the satellite. The task is then to construct the three motion maps  $\mathbf{V}_E$ ,  $\mathbf{V}_N$ , and  $\mathbf{V}_V$  from the known  $\mathbf{V}_{\text{SRS}}$  image (an interferogram) and sparse values of  $\mathbf{V}_E$ ,  $\mathbf{V}_N$ , and  $\mathbf{V}_V$  (GPS observations). For computational convenience, we

rewrite the three-dimensional equation (1) as the two equivalent two-dimensional terms

$$V_{\text{SRS}_k} = -[V_{L_k}, V_{V_k}][u_L, u_V]^T, \quad \forall k, \quad (2)$$

where

$$u_L = \sqrt{u_E^2 + u_N^2} \quad (3)$$

$$V_{L_k} = \frac{[V_{E_k}, V_{N_k}][u_E, u_N]^T}{u_L}, \quad \forall k. \quad (4)$$

The second term  $V_{L_k}$  is the deformation in the horizontal look direction of the satellite. The geometry of equation (2)

**Table 1.** Characteristics of the InSAR Interferograms

	Master Orbit	Date of Observation	Slave Orbit	Date of Observation	Elapsed Time, years	Altitude of Ambiguity $h_a$ , m
Figure 2a	5565	8 Aug. 1992	10575	24 July 1993	0.96	59.0
Figure 2b	5565	8 Aug. 1992	21941	25 Sept. 1995	3.13	43.6
Figure 2c	5565	8 Aug. 1992	7278	9 Oct. 1996	4.17	22000
Figure 2d	10575	24 July 1993	21941	25 Sept. 1995	2.17	166.0

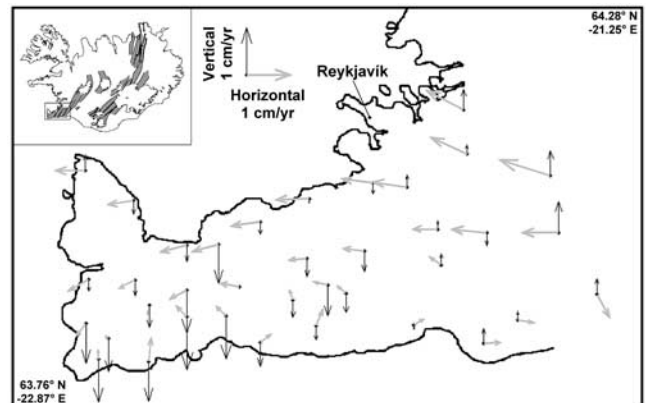


**Figure 3.** Average horizontal (dark) and vertical (light) displacement rates in the period from 1993 to 1998, measured by GPS (GPS locations are shown as black points). GPS data from *Hreinsdóttir* [1999].

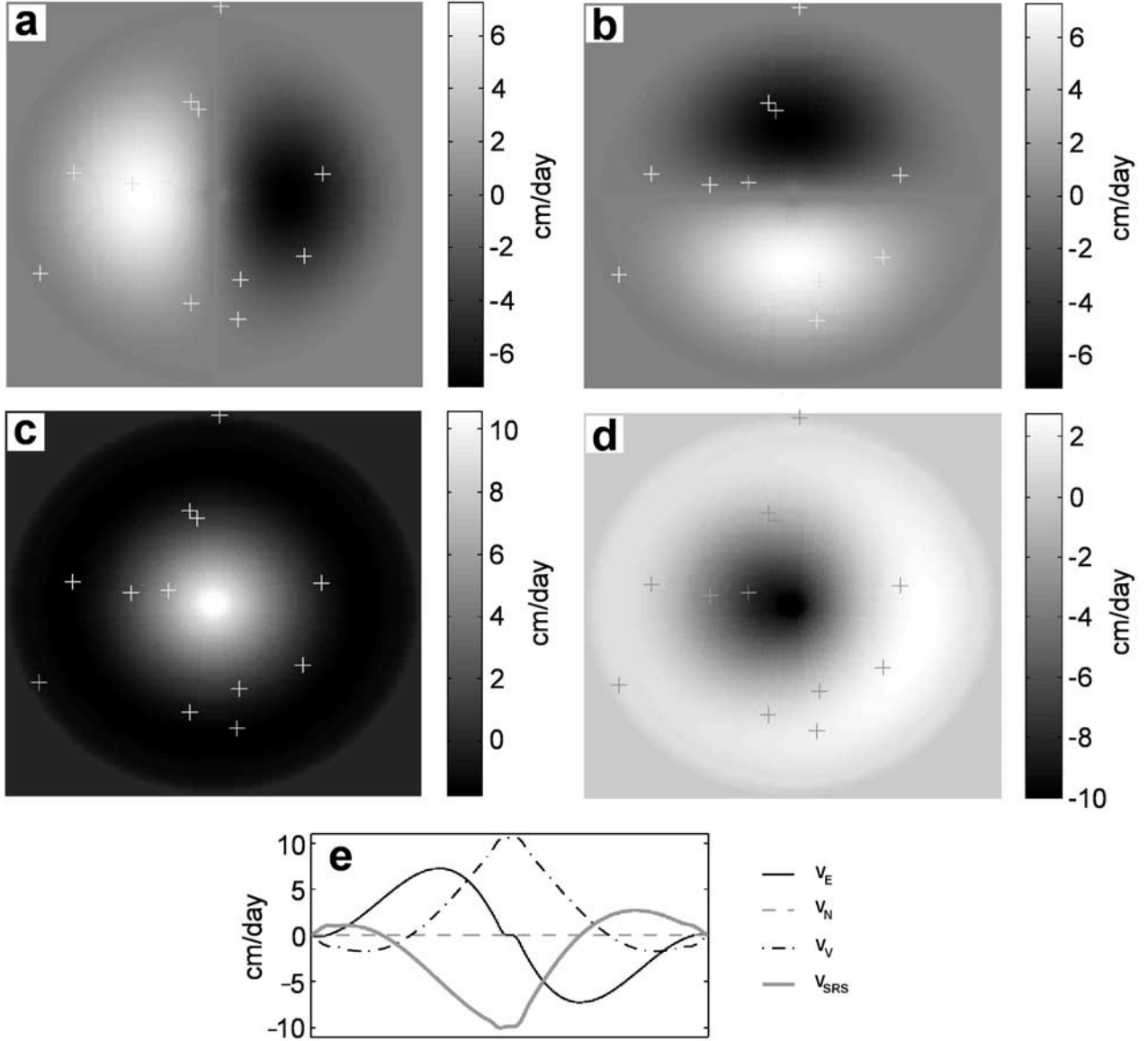


**Figure 4.** Synthetic motion field at an ice cauldron in cm/day, on  $164 \times 164$  pixels grid. The (a) east, (b) north, and (c) vertical motion maps; (d) corresponding unwrapped interferogram, assuming unit vector from ground to satellite given by equation (17). (e) Profiles along line 82 (central line) of the images in Figures 4a, 4b, 4c, and 4d. Assumed GPS locations for testing are shown as pluses.

is explained in Figure 5. Initially, one can use equation (2) as a basis to infer  $V_V$  and  $V_L$ . Then the east and north motion maps,  $V_E$  and  $V_N$  can be found by utilizing equation (4) or by rewriting equation (1) as

$$V_{SRSk} + u_V V_{V_k} = -[V_{E_k}, V_{N_k}][u_E, u_N]^T, \quad \forall k. \quad (5)$$

A general form of equations (2) and (5) is written

$$y_{1k} = -[x_{1k}, x_{2k}][u_1, u_2]^T, \quad \forall k, \quad (6)$$

where  $y_{1k}$  is known for all pixels  $k$ ,  $x_{1k}$  and  $x_{2k}$  are only known at sparse locations and  $u_1$  and  $u_2$  are constants. By using equation (6), the problem of optimizing the three motion maps in equation (1) is simplified to optimization of the two motion maps  $x_1$  and  $x_2$ . Hence the same opti-

mization algorithm can be used when optimizing  $x_1 = V_L$  and  $x_2 = V_V$  in equation (2), and  $x_1 = V_E$  and  $x_2 = V_N$  in equation (5) (see sections 5.2 and 5.3). This simplifies the optimization algorithm, since only two instead of three motion maps are optimized at the same time. This does though require  $V_L$  and  $V_V$  to be optimized previous to  $V_E$  and  $V_N$ .

#### 4. Markov Random Field Regularization and Simulated Annealing Optimization

[11] We use a MRF model to regularize the construction of the  $x_1$  and  $x_2$  motion maps in equation (6). The regularization is optimized with a simulated annealing iteration process. In MRF regularization, an optimal image  $x$  is interpreted as a realization of a random field  $X$ . Here a maximum a

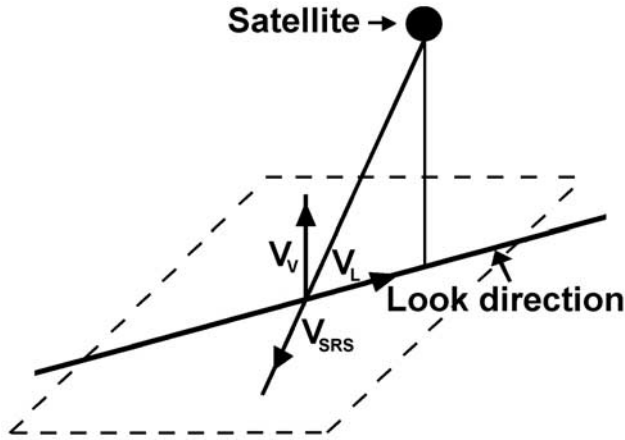


**Figure 5.** The geometry of equation (2).  $V_V$  and  $V_L$  are the vertical and horizontal look direction motion fields, respectively.

posteriori (MAP) estimate is used to represent an optimal realization image  $\mathbf{x}$  for a given image  $\mathbf{y}$  [e.g., *Carstensen, 1992; Li, 1995*]. The MAP estimation is given as

$$\hat{\mathbf{x}} = \arg \max_{\mathbf{x}} P(\mathbf{X} = \mathbf{x} | \mathbf{Y} = \mathbf{y}). \quad (7)$$

For convenience  $P(\mathbf{X} = \mathbf{x})$  will be written as  $P(\mathbf{x})$  when expressing the likelihood. The Bayesian theorem [e.g., *Ross, 1987, p. 20*] gives

$$P(\mathbf{x} | \mathbf{y}) = \frac{P(\mathbf{x})P(\mathbf{y} | \mathbf{x})}{P(\mathbf{y})} \propto P(\mathbf{x})P(\mathbf{y} | \mathbf{x}), \quad (8)$$

where  $P(\mathbf{x})$  represent prior expectations about the random field  $\mathbf{X}$  (e.g., assumption of having smoothly varying motion field and/or constraints given by physical models of surface motions) and  $P(\mathbf{y} | \mathbf{x})$  is the likelihood of the image  $\mathbf{y}$  given the image  $\mathbf{x}$  (the relation to the observations).

[12] A very important property of a Markov random field  $\mathbf{X}$  is that it is defined with respect to its neighborhood system [Carstensen, 1992, p. 81; Li, 1995, p. 11], such that a pixel value on an image grid is assumed to be conditionally dependent on its neighboring pixels only. This is the Markov property, which gives a local definition of the random field. The Markov property is utilized when a simulated annealing is used to optimize the MRF regularization, which results in a very effective image optimization process. By using the Hammersley-Clifford theorem [Besag, 1974; Carstensen, 1992, p. 83; Li, 1995, p. 14], the density function in equation (8) can be written as the Gibbs random field

$$\begin{aligned} P(\mathbf{x} | \mathbf{y}) &= P_T(\mathbf{x} | \mathbf{y}) \propto \exp\left(-\frac{1}{T}U(\mathbf{x} | \mathbf{y})\right) \\ &= \exp\left(-\frac{1}{T}U_1(\mathbf{x})\right)\exp\left(-\frac{1}{T}U_2(\mathbf{y} | \mathbf{x})\right) \\ &= \exp\left(-\frac{1}{T}(U_1(\mathbf{x}) + U_2(\mathbf{y} | \mathbf{x}))\right), \end{aligned} \quad (9)$$

where  $U(\mathbf{x} | \mathbf{y})$  is an energy function defined with respect to the neighborhood structure of the image  $\mathbf{x}$  (i.e.,  $U_1(\mathbf{x})$ ) and

the relationship of the image  $\mathbf{x}$  to the image  $\mathbf{y}$  (i.e.,  $U_2(\mathbf{y} | \mathbf{x})$ ), and  $T$  is a temperature. The Hammersley-Clifford theorem gives a global definition of the random field, and hence the MRF modeling can be regarded as defining a suitable energy function that takes its minimum energy stage for the optimal realization image.

[13] As  $T \rightarrow \infty$  the distribution in equation (9) becomes uniform among all possible energy states and as  $T \rightarrow 0$ , the distribution becomes uniform among the minimum energy states. The simulated annealing optimization can be described as a sampling of the density in equation (9), where the temperature  $T$  starts at some ‘‘high’’ value  $T_0 > 0$  and falls toward 0 during the iteration steps. If the temperature is lowered slowly enough, then equation (9) will assign the maximum probability to the MAP image [Geman and Geman, 1984]. One of the great advantages of using the simulated annealing optimization process is its relatively low risk of running into a local minimum compared to other optimization algorithms.

## 5. Construction of Motion Maps

[14] The construction process is started with initial motion maps created from interpolated GPS observations. The motion maps are then optimized further with MRF regularization and the simulated annealing algorithm.

### 5.1. Initial Motion Maps

[15] The initial motion maps are used as initial guesses before optimizing the 3-D motion field with the MRF regularization. Various methods exist for interpolation of sparse data [e.g., *Williams et al., 1998*]. The effectiveness of each method may depend on the characteristics of the sparse data. A reasonable choice of interpolation method needs to be considered with respect to each sparse data set. Here we will only demonstrate the method selected to interpolate the sparse data given in this paper and discuss some other possible alternatives.

[16] Several interpolation methods were tested for the sparse GPS data from the Reykjanes Peninsula. We found ordinary kriging algorithm given by *Gudmundsson* [2000, pp. 24–27] to be simple and appropriate (Figure 6). Kriging algorithms use geostatistical measurements to find an optimal set of weights used for the interpolation, calculated from a semivariogram (inverse related to the covariance) estimated from the data (Figures 6a, 6c, and 6e) [e.g., *Journel, 1989; Nielsen, 1998*]. The ordinary kriging algorithm requires the motion field to be both first and second order stationary [e.g., *Nielsen, 1998*], and the estimated semivariograms of each of the three GPS components to be fitted with a Gaussian semivariogram model [Gudmundsson, 2000, p. 25]. The Gaussian semivariogram model includes a preconception about the shape of the semivariogram (how the amplitude of the semivariogram ( $\gamma$ ) increases with distance). As seen from the GPS vectors (Figures 3 and 6) the motions at the Reykjanes Peninsula are east-west oriented and anisotropic. Furthermore, the vertical motions are partly localized, e.g., with some local subsidence at Svartsengi (Figure 1) [Vadon and Sigmundsson, 1997]. Hence the motion field is in general not stationary, and thus the averaged semivariograms (Figure 6) do not produce the appropriate shape that is needed for the Gaussian semi-

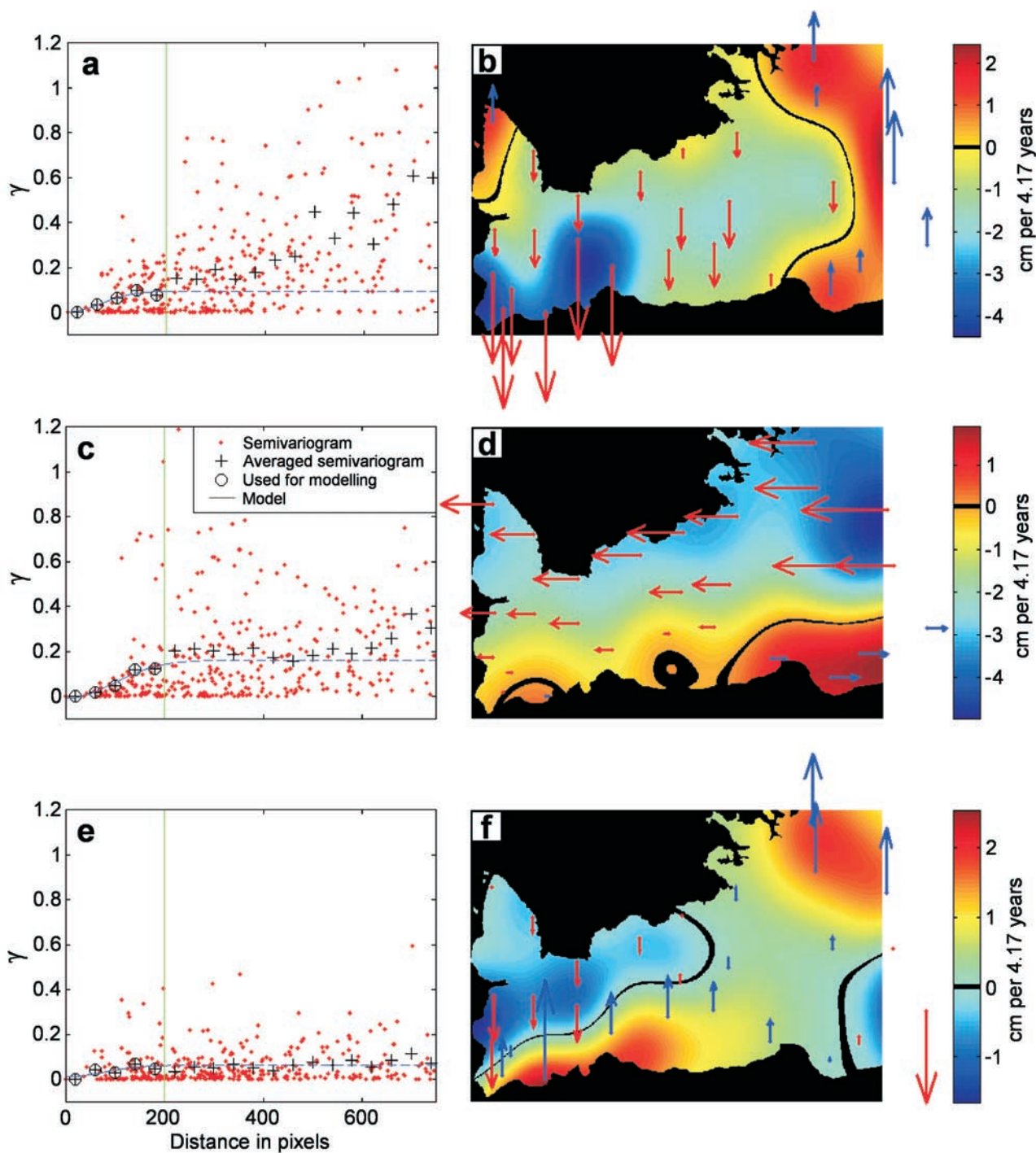


**Figure 6.** Semivariograms and results of kriging time-scaled GPS observations at the Reykjanes Peninsula. (a), (c), (e) Semivariogram scatterplot (red dots, inversely related to the covariance) derived from the vertical, east, and north components, respectively, of the GPS measurements of the 3-D motion field. Black pluses show results of averaging the scatterplot over a cross section of 20 pixels or  $\sim 1.8$  km. Only the circled pluses to the left of the green line (radius of 200 pixels or  $\sim 18$  km) were used to create the Gaussian semivariogram model (blue line) used for the kriging. (b), (d), (f) Kriging of sparse GPS measured vertical, east, and north motions, respectively. The sparse GPS measurements used for the interpolations are shown as vectors imprinted in Figures 6b, 6d, and 6f.

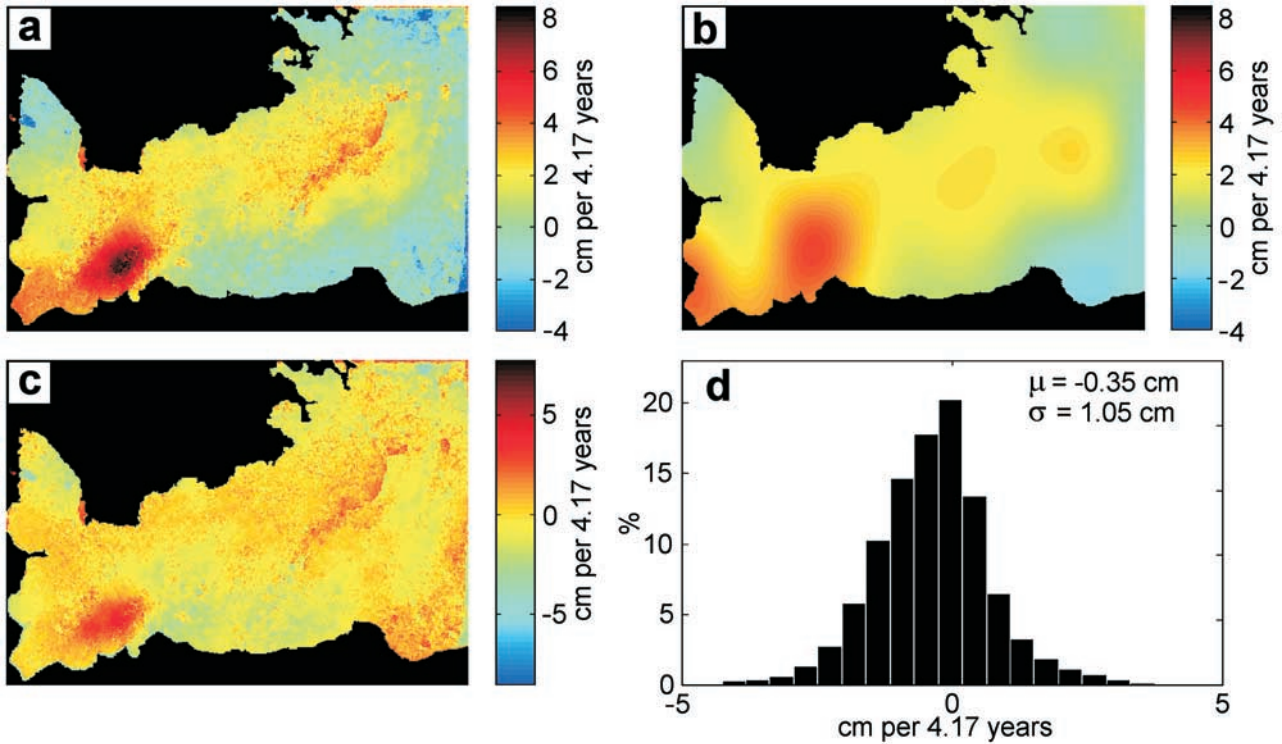


**Figure 7.** Comparison of the 4.17 years InSAR observation and the kriged GPS observations in Figure 6. (a) 4.17 years InSAR interferogram. (b) The kriged vertical, east, and north motion maps in Figure 6, projected into the slant range of the SAR satellite by using equation (1). (c) Residual errors between the InSAR interferogram in Figure 7a and the kriged and projected GPS observations in Figure 7b. (d) Normalized histogram of the residual errors in Figure 7c, and the mean value ( $\mu$ ) and standard deviation ( $\sigma$ ) of the residuals.

variogram model. However, the averaged semivariograms strongly indicate that the motion field is approximately first and second order stationary within a distance of at least 200 pixels ( $\sim 18$  km) from any arbitrary chosen location (point) at the Reykjanes Peninsula area. Hence an appropriate shape for the Gaussian semivariogram modeling can be achieved by only using semivariogram data within a distance of 200 pixels, as demonstrated in Figure 6.

[17] Figures 6b, 6d, and 6f show the result of ordinary kriging of the sparse GPS observations from the Reykjanes Peninsula. The spatial consistency of the GPS data is preserved in the kriged motion maps. Furthermore, both the east-west tendency of the horizontal motions and the localized subsidence pattern at Svartsengi appears to be preserved. Accurate interpolation of the subsidence pattern at Svartsengi is also supported by previous studies of the motion field at the area [Vadon and Sigmundsson, 1997]. Figure 7 shows an example of consistency between the interpolated GPS data and InSAR data. The good agreement of the two independent complementary data sets indicates a successful interpolation of the sparse GPS data.

[18] The ordinary kriging algorithm may not always be applicable. This was the case in the study of ice flow by Gudmundsson *et al.* [2002b], where motions were highly anisotropic and localized. In their case, both time series of digital elevation maps (DEMs) of the ice surface and aerial photographs were available. Thus they found it appropriate to use cubic spline fits of available sparse ground observations,

together with knowledge of the surface patterns from the aerial photographs and by assuming smoothly varying horizontal ice flow parallel to flow lines with the aid of the DEMs. Another type of localized and anisotropic surface movements are discontinuities because of seismic or aseismic deformation. Often, there exists a physical model that describes the general patterns of such motions. One possibility is to remove the model from the GPS observations, interpolate the residuals (e.g., with the ordinary kriging algorithm) and add back in the model. Such residuals are expected to be approximately a stationary random field, which is the most appropriate form for kriging algorithms. Furthermore, such models can be considered as prior expectations in the MRF regularization as discussed further in section 5.2.

## 5.2. Energy Functions

[19] A general form of a total energy function used to optimize the two motion maps  $\mathbf{x}_1$  and  $\mathbf{x}_2$  in equation (6) can be written

$$\begin{aligned}
 U(\mathbf{x}_1, \mathbf{x}_2 | \mathbf{y}) &= U_1(\mathbf{x}_1, \mathbf{x}_2) + U_2(\mathbf{y} | \mathbf{x}_1, \mathbf{x}_2) \\
 &= U_{11}(\mathbf{x}_1) + U_{22}(\mathbf{x}_2) + U_2(\mathbf{y} | \mathbf{x}_1, \mathbf{x}_2), \quad (10)
 \end{aligned}$$

where the former step is an extension of the energy functions in equation (9), and the later step is achieved by assuming independence between the likelihoods of  $\mathbf{x}_1$  and

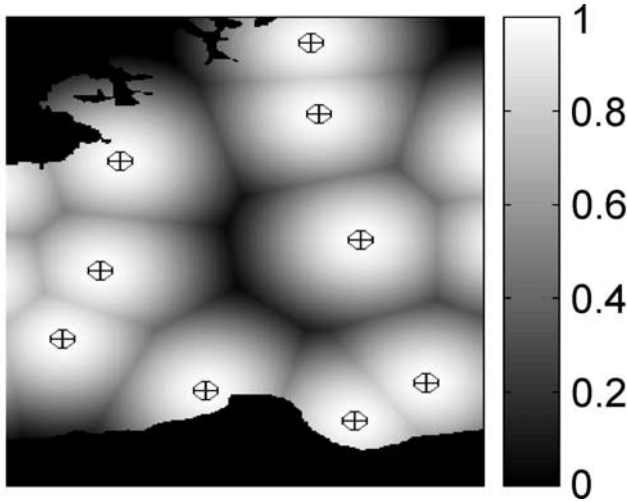


**Figure 8.** A subregion of an uncertainty image calculated for the kriging result in Figure 6a. GPS locations are shown as  $\oplus$ .

$\mathbf{x}_2$ .  $U_{11}(\mathbf{x}_1)$  and  $U_{22}(\mathbf{x}_2)$  are then related to the neighborhood structure of  $\mathbf{x}_1$  and  $\mathbf{x}_2$ , respectively, and  $U_2(\mathbf{y}|\mathbf{x}_1, \mathbf{x}_2)$  expresses the relationship of the two-dimensional motion field to the unwrapped InSAR image  $\mathbf{y}$  as given in equation (6). An energy function used to optimize equation (6) is given as

$$U_2(\mathbf{y} | \mathbf{x}_1, \mathbf{x}_2) = \gamma_2 \sum_n \left( y_n + [x_{1n}, x_{2n}] [u_1, u_2]^T \right)^2, \quad (11)$$

where  $n$  is a pixel number and  $\gamma_2$  is a constant.

[20] Additional constraints we invoke are the smoothness of the first derivatives of  $\mathbf{x}_1$  and  $\mathbf{x}_2$ , implemented as a penalization on the second derivative [e.g., Li, 1995, pp. 47–48], with the approximations

$$U_{11}(\mathbf{x}_1) = \gamma_{11} \sum_i \sum_j (x_{1i-1,j} + x_{1i+1,j} - 4x_{1i,j} + x_{1i,j-1} + x_{1i,j+1})^2 \quad (12)$$

$$U_{22}(\mathbf{x}_2) = \gamma_{22} \sum_i \sum_j (x_{2i-1,j} + x_{2i+1,j} - 4x_{2i,j} + x_{2i,j-1} + x_{2i,j+1})^2, \quad (13)$$

where  $i, j$  are the row and column numbers, respectively, and  $\gamma_{11}$  and  $\gamma_{22}$  are constants. By using equations (12) and (13), we have assumed the motion field to be smoothly varying. The smoothness requirements were the only prior expectations about the random field used in this paper. Here, it serves the important purpose of preserving the correlated relationship of the image pixel values. The  $U_1$  term in equation (10) may consist of various types of prior expectations. As an example, in study of ice flow, Gudmundsson et al. [2002b] used an assumption of having horizontal ice flow parallel to the flow lines at the surface, implemented with aid of digital elevation map. This additional prior expectation was easily incorporated into

the process presented in this paper, simply by using  $U_1$  as a superposition of equations (12) and (13), and the constraint of having the horizontal flow field parallel to the flow line at the surface. Furthermore, one could also utilize physical models of surface motions as constraints in  $U_1$ . Prior expectations derived from physical models were not considered in this paper.

[21] The energy function in equation (10) utilizes the relationship of the motion field images to the known image  $\mathbf{y}$ . Sparse values of the motion field images  $\mathbf{x}_1$  and  $\mathbf{x}_2$  are known from the GPS observations and are used to initialize the process. The interpolated initial motion maps (the GPS observations) can also be utilized into the MRF models by extending equation (10) as

$$\begin{aligned} U(\mathbf{x}_1, \mathbf{x}_2 | \mathbf{y}, \mathbf{x}_{11}, \mathbf{x}_{12}) &= U_1(\mathbf{x}_1, \mathbf{x}_2) + U_3(\mathbf{y}, \mathbf{x}_{11}, \mathbf{x}_{12} | \mathbf{x}_1, \mathbf{x}_2) \\ &= U_{11}(\mathbf{x}_1) + U_{22}(\mathbf{x}_2) + U_2(\mathbf{y} | \mathbf{x}_1, \mathbf{x}_2) \\ &\quad + U_{11}(\mathbf{x}_{11} | \mathbf{x}_1) + U_{12}(\mathbf{x}_{12} | \mathbf{x}_2), \end{aligned} \quad (14)$$

where  $\mathbf{x}_{11}$  and  $\mathbf{x}_{12}$  are the estimated initial values of  $\mathbf{x}_1$  and  $\mathbf{x}_2$ , respectively. As in equation (10), independence is assumed between the likelihoods of  $\mathbf{x}_1$  and  $\mathbf{x}_2$ , which leads to the final step in equation (14).

[22] The expected spatially variable accuracy of the interpolation (kriging) results can be incorporated in the regularization by introducing an ‘‘uncertainty image’’  $\mathbf{u}$ . Here we use a method introduced by Gudmundsson [2000, p. 34] to create the uncertainty image along with the kriging of the sparse motion field measurements. In his method, the kriging results are expected to be most accurate at, and close to, pixels corresponding to the GPS locations but become more uncertain with distance from them. No uncertainty is assigned to pixels with GPS observations and the certainty then decreases away from them. In the uncertainty image, a value of one means no uncertainty and a value of zero means no certainty (Figure 8). The spatial accuracy of the interpolation may also depend on variable uncertainty assigned to each GPS vector. It is possible to incorporate those variable errors in the uncertainty image, by assigning suitable uncertainty value to pixels with GPS observations. The initial values and the uncertainty image are utilized into the MRF regularization by penalizing the motion maps for deviating from the initial results. The penalization is then weighted with the uncertainty image. This is done by using the energy terms

$$U_{11}(\mathbf{x}_{11} | \mathbf{x}_1) = \gamma_{11} \sum_n \left( w_{1n} (x_{11n} - x_{1n}) \right)^2 \quad (15)$$

$$U_{12}(\mathbf{x}_{12} | \mathbf{x}_2) = \gamma_{12} \sum_n \left( w_{2n} (x_{12n} - x_{2n}) \right)^2 \quad (16)$$

for the motion field images  $\mathbf{x}_1$  and  $\mathbf{x}_2$ , respectively, where  $n$  is pixel number,  $x_{11n}$  and  $x_{12n}$  are the initial values at the pixel  $n$ ,  $w_{1n}$ , and  $w_{2n}$  are the estimated uncertainty of the initial values at the pixel  $n$  and  $\gamma_{11}$  and  $\gamma_{12}$  are constants. Because of the uncertainty images, the penalization in equations (15) and (16) becomes strongest at and close to pixels with GPS values and decreases with distance from them. The energy function in equation (14) has the

advantage of utilizing both the relationship of the motion maps to InSAR and GPS observations.

### 5.3. Simulated Annealing Optimization

[23] The simulated annealing process used for the optimization of the two realization images  $\mathbf{x}_1$  and  $\mathbf{x}_2$  is given in algorithm 1 in Appendix A. Here, the optimization is separated into two steps. First  $\mathbf{x}_1$  is updated for given  $\mathbf{x}_2$ , and then  $\mathbf{x}_2$  for a given  $\mathbf{x}_1$ . Then these steps are repeated until a satisfactory result is achieved. The energy function  $U$  is given by either equation (10) or (14). The algorithm uses a nonrecursive update of the pixel values [e.g., *Gudmundsson, 2000, p. 35*]. The MRF model favors low energy states by associating them with high probabilities. The Markov property of the random field is utilized when calculating the ratio of the image probability states with and without updated pixel value (steps 4 and 10 in algorithm 1). Because of the Markov property, all terms in the probability formulation not directly related to the pixel under consideration disappear. This is evident when implementing the associated energy functions in section 5.2 into the calculation of the image probability ratio in steps 4 and 10, i.e., all terms in the summation in equations (11), (12), (13), (15), and (16) not directly related to the updated pixel value cancel out in the probability ratio. Furthermore, the energy terms in equations (13) and (16) (energy terms not related to  $\mathbf{x}_1$ ) cancel out in step 4 and in equations (12) and (15) (energy terms not related to  $\mathbf{x}_2$ ) in step 10. In the algorithm,  $\mu[0,1]$  is a random number ranging from 0 to 1, selected from a uniform random generator. This simulated annealing algorithm chooses a new energy stage if the probability ratio is larger than random number within the  $[0,1]$  interval. This allows the algorithm to explore various combinations of the motion maps, and hence avoid local minima. As  $T \rightarrow 0$ , the effects from the random generator vanish. The constant cool in algorithm 1 establishes the temperature fall. After full annealing, the algorithm selects the motion maps with the highest probability.

### 5.4. Parameters

[24] Because the energy functions in section 5.2 represent different types of quantities, the ratio of the  $\gamma$  coefficients represents combination of both scaling and weighting of each of the energy terms in the optimization. Furthermore, evaluation of suitable values for these parameters is not a simple task. By using various experiments, we found  $\gamma_2 = 10$  in equation (11),  $\gamma_{11} = 1$  and  $\gamma_{22} = 2$  in equations (12) and (13), respectively, and  $\gamma_{11} = \gamma_{12} = 10$  in equations (15) and (16), to work well for our data. Relationship of the motion maps to the InSAR observations is reflected in equation (11), i.e., projection of the motion maps on a unit vector is known at all pixels. Thus, the energy term in equation (11) is given a relatively strong weight in the optimization. An infinite set of solutions exists for equation (11). Hence, we use as an additional constraint (a prior expectation about the motion field) an assumption of having a smoothly spatial varying motion field (equations (12) and (13)). Those smoothness requirements also reduce the effects of high frequency noise errors in the InSAR data. A smoothly varying motion field is not always the case, e.g., when there are discontinuities due to seismic deformation. Strong smoothness requirements can result in over-

smoothing of narrow deformation features. Here we keep the weights of equations (12) and (13) small but under the consideration of achieving acceptable spatial correlation in the output motion maps. The energy terms in equations (15) and (16) express the relationship of the output motion maps to the sparse GPS data. Those energy terms also tend to smooth the output data. The smoothing effects are though small compared to those of equations (12) and (13). Here we keep the constraint in equations (15) and (16) much weaker than in equation (11).

[25] The weights may depend on the nature of the data. *Gudmundsson et al. [2002b]* found the same values of  $\gamma_2$ ,  $\gamma_{11}$ , and  $\gamma_{22}$  to be suitable to optimize 3-D motion maps at the 1996 Gjalp eruption site in Vatnajökull, Iceland. Opposite to our GPS data, their sparse ground observations of the vertical, east, and north components of the motion field were not all conducted at the same locations. Because of this, it was better to use only half the values we use for  $\gamma_{11}$  and  $\gamma_{12}$  in that case. We use  $T_0 = 5$ ,  $\Delta x = 0.1$ , and cool = 0.99 in algorithm 1, and the process is terminated for  $T < 0.1$ .

### 5.5. Extracting Areas of Interest

[26] It is not always necessary to update all pixels within the motion maps during the simulated annealing optimization. Our study area is surrounded by an ocean, which contains no information on deformation. Those pixels are kept frozen in the simulated annealing optimization (not updated), which results in a faster process. A binary mask is used to extract areas of interest [*Gudmundsson, 2000, p. 19*]. The mask is created by thresholding the InSAR interferogram, followed by a morphological cleaning [e.g., *Conzales and Woods, 1993; Carstensen, 1998*] of the area of interest (the foreground). The mask is then utilized into the simulated annealing algorithm, where only pixels within the foreground area are updated during the iteration.

## 6. Results

[27] The  $164 \times 164$  pixel test case was used to test the image reconstruction process. The process was then used to infer motion maps to describe the three-dimensional motion field at the Reykjanes Peninsula. For the interferograms covering the Reykjanes Peninsula, the unit vector in equation (1) is given as [*Vadon and Sigmundsson, 1997*]

$$[u_E, u_N, u_V] \approx [0.34, -0.095, 0.935]. \quad (17)$$

The same unit vector is assumed for the test case.

### 6.1. Synthetic Ice Flow Motion

[28] The uncertainty of the 3-D motion maps is expected to be reduced after an optimization of equation (10) or (14). Here, we use the  $164 \times 164$  pixel error-free synthetic interferogram to show how the initial errors of the 3-D motion maps can be reduced with the optimization scheme. Estimation of errors for the test case is given in Table 2. The errors are estimated as the mean ( $\mu$ ) and the standard deviation ( $\sigma$ ) of the residuals between the correct and estimated motion maps. Table 2 shows the errors of kriging the sparse located GPS observations shown in Figure 4, the result of using only the relationship of the motion maps to the InSAR observations in the MRF regularization in equation

**Table 2.** Estimate of Errors in the Construction of Motion Maps for the Test Case in Figure 4<sup>a</sup>

	Vertical	East	North	Slant Range
		<i>Kriging Error</i>		
$\mu$	0.07	0.18	0.32	-0.09
$\sigma$	0.44	1.03	0.66	0.41
		<i>Simulation Error by Optimizing Equation (10)</i>		
$\mu$	-0.02	0.13	0.23	0.003
$\sigma$	0.29	0.85	0.57	0.05
		<i>Simulation Error by Optimizing Equation (14)</i>		
$\mu$	-0.02	0.11	0.24	-0.001
$\sigma$	0.28	0.83	0.56	0.10

<sup>a</sup>Kriging errors and errors when using equations (10) and (14) (in cm/d). No errors are included in the synthetic interferogram and the GPS measurements.

(10) and the result of using also the relationship to the GPS observations in the MRF regularization in equation (14). For the test case in Table 2, the reduction of  $\sigma$  (error reduction) by an optimization of equations (10)/(14) is  $\sim 34\%/36\%$ ,  $\sim 17\%/19\%$  and  $\sim 14\%/15\%$  for the vertical, east, and north motion maps, respectively. The results are slightly better when optimizing equation (14) than equation (10).

[29] The observed vertical GPS component is often much less reliable than the observed horizontal GPS components. On the other hand, vertical component of any motion field gives the highest contribution to the InSAR signal (see equation (17)), i.e. is the largest component in the InSAR signal. The complementary information of the two data sets compensate each other when optimizing equation (10) or (14). This is reflected in Table 2, where the highest error reduction is achieved for the vertical motion map. Our experiments show that the optimization result can be very dependent on the quality and certainty of the input data. For example, the possibility of detecting “narrow features” in the 3-D motion field is highly dependent on the density of the GPS network. Despite this, it is clear that the errors of the initial motion maps can be reduced by using “low error” InSAR data and the presented MRF regularization.

[30] Here we have not included errors in the synthetic data when estimating the error reduction in Table 2, since the purpose is only to evaluate the optimization of equations (10) and (14). Furthermore, errors can vary highly from one data set to another. Large errors in GPS observations increase the errors in the initial 3-D motion maps. Because of the relationship of the 3-D motion maps to interferometric observations in equation (11), the ratio of optimized to initial errors of the 3-D motion maps decreases with increased GPS errors (more error reduction). On the other hand, increased errors in the interferometric observation are expected to increase the ratio of optimized to initial errors (less error reduction). Thus the error reduction in presented in Table 2 is expected to be lower than if errors were included in the synthetic GPS observations and higher than if errors were included in the synthetic interferometric observations.

## 6.2. Reykjanes Peninsula

[31] Before inferring high-resolution motion maps for the three-dimensional motion field at the Reykjanes Peninsula from combined GPS and InSAR observations, the two

complementary data sets need to be made time-consistent. The InSAR interferograms may also include residual orbital errors. Here the orbital errors are assumed to be of the form of a linear phase plane. The GPS data were analyzed with precise orbit information [Hreinsdóttir et al., 2001], and therefore the results are not expected to include significant systematic errors. Hence they can be used to reduce orbital errors in the InSAR data [Gudmundsson, 2000, pp. 21–29 and p. 59]. The GPS derived motion vectors are projected into the slant range direction toward the satellites, and time scaled to fit the elapsed time interval represented by the InSAR data. The sparse GPS estimates of the slant range shift are then used to find a least squares fit of the residual orbital phase plane. The phase plane is then eliminated from the InSAR interferogram. When the InSAR and GPS observations represent different elapsed time intervals, possible time variability in the ground movements and a poor estimate of some of the vertical motions vectors from GPS has to be considered. Our experiments have shown that a good consistency is obtained between a majority of the time-scaled GPS motion vectors and the phase corrected InSAR data from the Reykjanes Peninsula. Here we have, however, rejected a few GPS observations that both include high uncertainties (section 2.1) and are inconsistent with the InSAR observations, before inferring the motion maps.

[32] Figures 6 and 9 show the result of inferring motion maps ( $450 \times 750$  pixel) by using the GPS observations and the 4.17 years InSAR observations from the Reykjanes Peninsula (Table 1 and Figure 2). Figure 6 shows the result of kriging the time-scaled GPS observations. Figure 9 gives the result of applying MRF regularization on the kriged motion maps, both by optimizing only the relationship to the InSAR observation given in equation (10), and by optimizing the relationships to both the InSAR and GPS observations given in equation (14). In both cases the resulting motion maps have similar patterns. It is evident by comparing the constructed motion maps in Figure 9 to the 4.17 years InSAR interferogram (Figure 2) that the motion maps inherit more details from the InSAR observation when using optimization of the energy in equation (10). The results are then more influenced by the kriging results (the GPS observations) when optimizing equation (14), especially the north motion field. Here this is of advantage since the north motion field is mainly inferred from the GPS observations due to its low contribution to the slant range shift (see equation (17)).

[33] Plots of line 300 from the kriged and MRF regularized motion field images are given in Figure 10. The effects of using the spatially varying energy term in equations (15) and (16), that relates the MRF regularized results to the kriged results, is evident from those profiles. A higher correlation is achieved between the profile patterns in Figure 10c than Figure 10b, to the initial profile patterns in Figure 10a. Also, these energy terms affect the north motion field the most and the vertical motion field the least; the motion field with the lowest and highest contribution to the InSAR observation, respectively (see equation (17)). Figure 11 shows the difference between line 300 in the 4.17 years InSAR interferogram and the profiles in Figure 10 projected into the slant range of the satellite. The difference shows that the 3-D motion signals, projected into the slant range of the satellite, look more like the InSAR signal when only

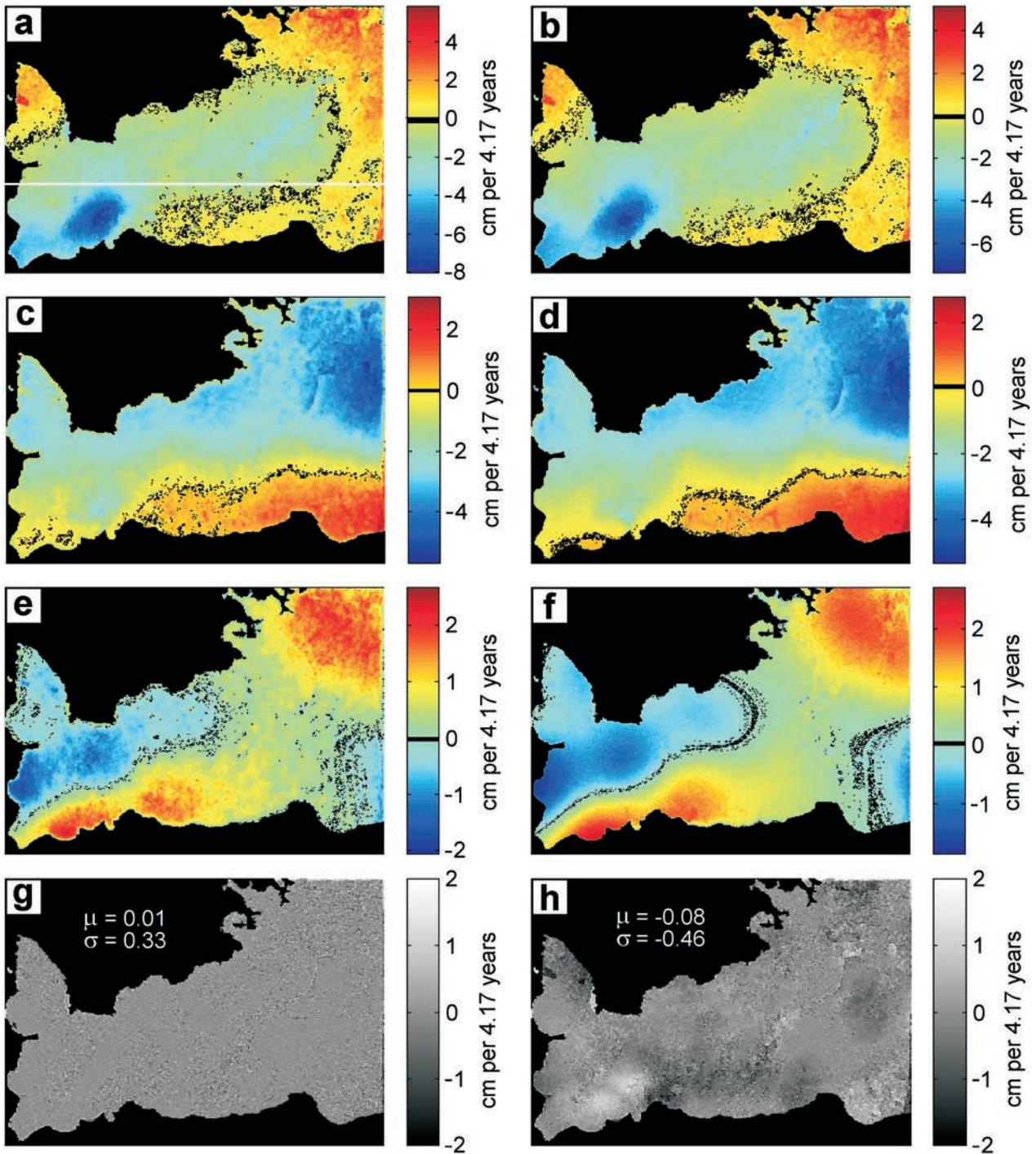


**Figure 9.** Ground movements at the Reykjanes Peninsula inferred by using the GPS measurements and 4.17 years interferogram. The results are shown of using only the relationship to the InSAR observation in equation (10), and the relationship to both the InSAR and GPS observations in equation (14), in the MRF regularization. (a), (c), (e) The vertical, east, and north motion maps, respectively, inferred by optimizing equation (10). (b), (d), (f) The same from optimizing equation (14). (g) Residual error between the 4.17 years interferogram and projection of the images in Figures 9a, 9c, and 9e into the slant range of the SAR satellite, and the mean value ( $\mu$ ) and standard deviation ( $\sigma$ ) of the residuals. (h) The same for the images in Figures 9b, 9d, and 9f. The white line in Figure 9a shows the location of the profiles in Figures 10 and 11 (row 300).

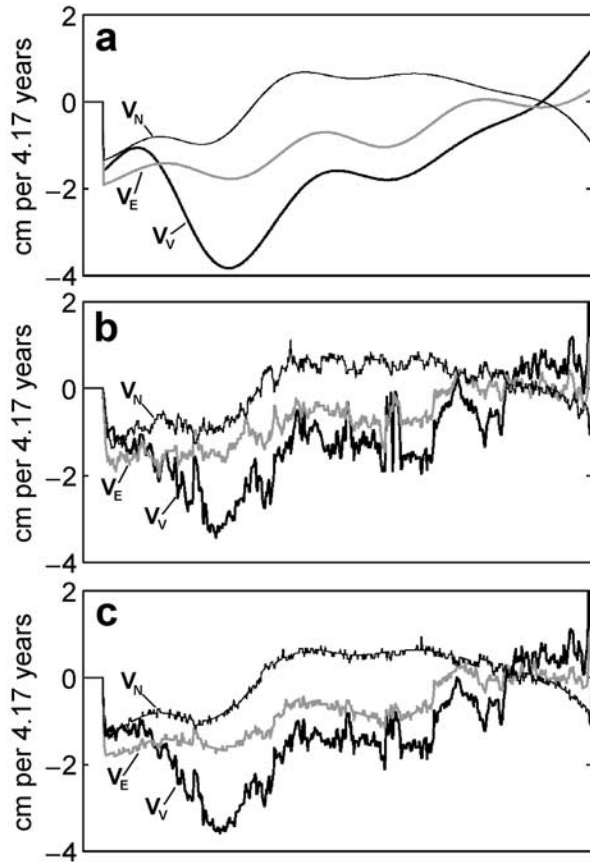


**Figure 10.** Row 300 out of the estimated  $450 \times 750$  pixels motion maps in Figures 6 and 9. See the profile location in Figure 9a. (a) The result from kriging, (b) result of using the MRF regularization that utilizes only the relationship to the InSAR observation in equation (10), (c) result of using the MRF regularization that utilizes both the relationship to the InSAR and GPS observations in equation (14).

optimizing equation (10) (Figure 11b) than equation (14) (Figure 11c). The signals in Figure 10a are more related to the signals in Figure 10c than in Figure 10b. Thus the difference in Figure 11a shows higher correlation to the difference in Figure 11c than in Figure 11b. The smoothing requirements in equations (12) and (13) tends to smooth the 3-D motion maps, which explains for example the power left in the shortest wavelengths of the residuals in Figure 11b.

## 7. Discussion

[34] The optimal solutions of equation (10) or (14) are ill-defined when the three-dimensional values are known only at sparse locations from GPS. Furthermore, “narrow features” in the 3-D motion field can only be detected if the input data include enough information about them. A key factor in that case is the density of the GPS points covering the narrow features. Denser GPS network means more accurate information and too sparse GPS observations can result in lack of information and oversmoothing of narrow features. Thus the result of optimizing a 3-D motion field can be highly dependent on the quality of the input data and

the spatial distribution of the GPS sites. Despite this, results on our synthetic interferogram of ice flow have shown that the errors in interpolated (e.g., kriged) motion maps can be reduced significantly by using a “low error” interferometric observations in the MRF regularization (Table 2). This is particularly true for the vertical motion field due to its high contribution to the interferometric signal.

[35] The purpose of the smoothness requirements in equations (12) and (13) is to preserve a spatial correlation of the motion field, and hence, make the optimal solution better defined. Often more prior expectation about the 3-D motion field can be included in the MRF regularization, e.g., expectations about flow directions [e.g., Gudmundsson *et al.*, 2002b] or utilization of physical models of the motion fields. More prior expectations results in better defined solution of the 3-D motion field. A smoothly varying motion field is not always the case, e.g., when there are discontinuities due to seismic deformation. If the GPS points are not dense enough to cover the discontinuity, and perhaps not enough spatial coverage of the InSAR data, then optimiza-

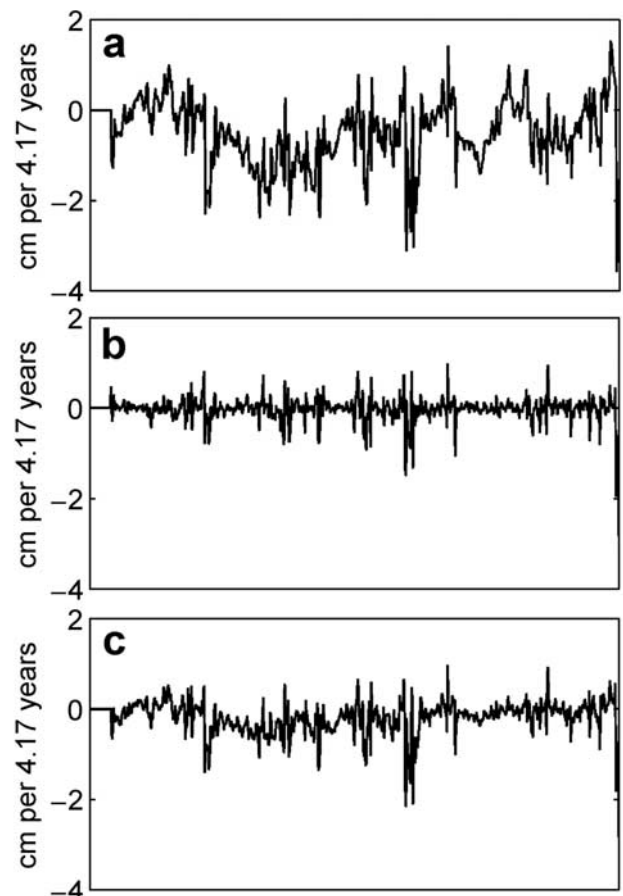


**Figure 11.** Residual errors between row 300 out of the  $450 \times 750$  pixels, 4.17 years, interferogram and projection of the motion field profiles in Figure 10 into the slant range. See the profile location in Figure 9a. (a) The residuals from kriging, (b) the residuals by using the MRF regularization that utilizes only the relationship to the InSAR observation in equation (10), (c) the residuals by using the MRF regularization that utilizes both the relationship to the InSAR and GPS observations in equation (14).

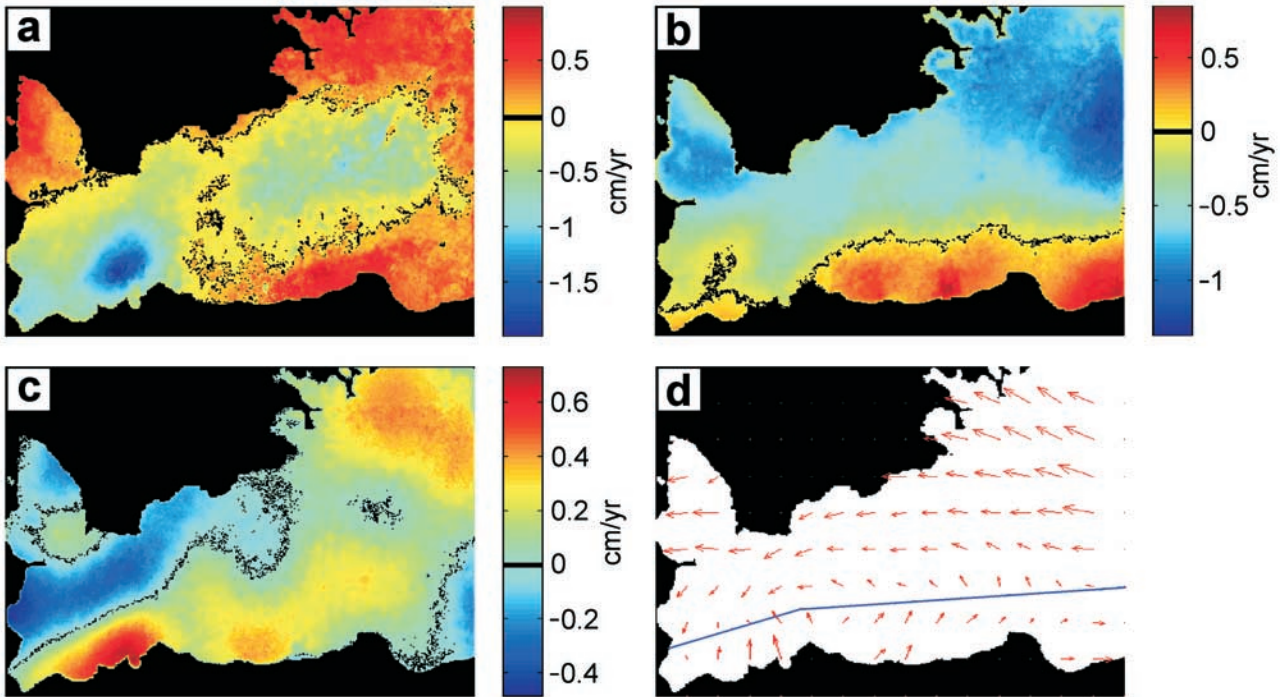


**Figure 12.** Estimated 1-year average motion field maps at the Reykjanes Peninsula. (a), (b) and (c) Average vertical, east and north motion maps, respectively, inferred by the 1992–1993, 1992–1995, 1992–1996, and 1993–1995 InSAR data, and the 1993–1998 GPS data. (d) Vector plot of the horizontal displacements in Figures 12b and 12c. The blue line in Figure 12d indicates the approximate location of the division line (no movements) between the east and west movements in the east motion map (see Figure 12b), ignoring the horizontal movements associated with the subsidence centered on the Svartsengi and Eldvörp geothermal area. This line is the approximate location of the central axis of the plate boundary.

tion of equation (10) or (14) would result in false over-smoothing of the discontinuity. As mentioned in section 5.4, the smoothness constraints are kept relatively weak compared to those that relate the optimized 3-D motion maps to the input InSAR and GPS observations. Thus the MRF regularization follows much more the information given by the observations than the smoothness requirements. Hence, if the input data include enough information about discontinuity or any other types of narrow features, then those features can be inferred in the 3-D motion maps. However, the smoothness constraints will always result in some false smoothness when optimizing equation (10) or (14) but on a negligible or small scale.

[36] Another point of concern is that the InSAR and GPS data may cover different time intervals, and then the possibility of a nonlinearity in deformation rates needs to be considered. For the Reykjanes Peninsula we have assumed the rates of deformation to be constant within our study period, as no large earthquakes have occurred. However, few GPS points were inconsistent with the interferograms. An explanation for this discrepancy is most likely a poor estimate of the motion components of deformation from GPS at some sites, especially of the vertical component, and some nonlinear temporal variation of the deformation field and noise of atmospheric or ionospheric origin, for some parts of the image area. Because of the flexibility of our algorithm, it is not necessary to have all the

deformation components measured at the same locations. For example, only the vertical component of the GPS observations, with both high uncertainties and inconsistency with the InSAR observations, could be rejected. Here the uncertainty of the GPS observations was not included in the optimization of the 3-D motion maps. An improvement of the optimization methodology could be to incorporate the known GPS uncertainties, e.g., with aid of the uncertainty images as explained in section 5.2.

[37] In cases when deformation rates can be expected to be constant, it is beneficial to average motion maps created from a series of interferograms, in order to more accurately infer long-term movements. Figure 12 represents such one-year average motion for the Reykjanes Peninsula, estimated by using the 1993–1998 GPS observations along with the 1992–1993, 1992–1995, 1992–1996, and 1993–1995 interferograms. The elapse times of these data are 5, 0.96, 3.13, 4.17, and 2.17 years, respectively. Motion maps were estimated independently for each of the four interferograms. The averages were then created by weighting the motion maps with their corresponding elapsed time intervals. Here we have only rejected the vertical component of the few uncertain GPS points that were inconsistent with both the InSAR images and neighboring GPS observations. Although separate interpretations of GPS and InSAR data from the area [Hreinsdóttir *et al.*, 2001; Vadon and Sigmondsson, 1997] have shown the main components of

deformation, the three-dimensional motion maps provide an unprecedented view of the three-dimensional deformation. The largest signals are plate movements causing large gradients in the east motion field, and circular subsidence centered on the Svartsengi and Eldvörp geothermal area (see Figure 1 for location). The north and east motion field images show also clearly that the subsidence is associated with horizontal movements toward the subsidence center, a pattern that is imprinted on the background plate movements. The location of central axis of the plate boundary, as estimated from the combined GPS and InSAR data (Figure 12d), is in good agreement with the location of the central axis as inferred from seismicity (see Figure 1 for location).

**8. Conclusion**

[38] A method and algorithm are provided to combine unwrapped interferograms, and GPS estimates of three-dimensional movements at sparse locations, in order to infer high-resolution three-dimensional surface motion maps. Sparsely located GPS measured surface movements are initially interpolated using ordinary kriging, thereby producing a value for east, north, and vertical component of movement for each pixel in an interferogram. MRF regularization and simulated annealing are then used to optimize the images using the InSAR and GPS data as constraints. MRF modeling is a flexible method that gives an opportunity to develop the optimization further if needed. If InSAR interferograms are available from both ascending and descending satellite passes, then these can be easily incorporated into the optimization, by adding an appropriate set of energy functions.

**Appendix A: Algorithm 1**

1. Choose initial images  $\mathbf{x}_1$  and  $\mathbf{x}_2$  (e.g., by kriging) and set the initial temperature  $T = T_0$ .
2.  $k = 1$ , where  $k$  is a pixel number.
3. Increase or decrease  $x_{1k}$  with equal probability by a value of  $\Delta x$ , which gives a new image  $\mathbf{x}'_1$ .
4. Calculate  $r_{1k} = [p_T(\mathbf{x}'_1)/p_T(\mathbf{x}_1)] = \exp \{-[U(\mathbf{x}'_1) - U(\mathbf{x}_1)]/T\}$ .
5. If  $r_{1k} > \mu[0,1]$ , then  $x_{1tk} = x'_{1k}$ ; otherwise  $x_{1tk} = x_{1k}$ .
6.  $k = k + 1$ , if  $k \leq M$ , go to step 3; otherwise, go to the next step ( $M$  is the total number of pixels).
7.  $\mathbf{x}_1 = \mathbf{x}_{1t}$ .
8.  $k = 1$ .
9. Increase or decrease  $x_{2k}$  with equal probability by a value of  $\Delta x$ , which gives a new image  $\mathbf{x}'_2$ .
10. Calculate  $r_{2k} = [p_T(\mathbf{x}'_2)/p_T(\mathbf{x}_2)] = \exp \{-[U(\mathbf{x}'_2) - U(\mathbf{x}_2)]/T\}$ .
11. If  $r_{2k} > \mu[0,1]$ , then  $x_{2tk} = x'_{2k}$ ; otherwise,  $x_{2tk} = x_{2k}$ .
12.  $k = k + 1$ , if  $k \leq M$ , go to step 9; otherwise, go to the next step.
13.  $\mathbf{x}_2 = \mathbf{x}_{2t}$ .
14.  $T = T \times \text{cool}$ , where  $\text{cool} < 1$  is a constant.
15. Go to step 2.

[39] **Acknowledgments.** This work was supported by European community grants ENV4-CT97-0536 + A6 to the PRENLAB-2 project and EVG1-CT-2001-00046 to the RETINA project, a special grant from the Icelandic government, and the Icelandic Research Council. We thank Sigrún Hreinsdóttir for making the GPS results from the Reykjanes

Peninsula available to us. Comments from two anonymous reviewers and an Associate Editor greatly improved the manuscript.

**References**

Besag, J., Spatial interaction and the statistical analysis of lattice systems, *J. R. Stat. Soc., Ser. B*, 36, 192–236, 1974.

Björnsson H., H. Rott, S. Gudmundsson, A. Fischer, A. Siegel, and M. T. Gudmundsson, Glacier-volcano interactions deduced by SAR interferometry, *J. Glaciol.*, 47(156), 58–70, 2001.

Bock, Y., and S. Williams, Integrated satellite interferometry in southern California, *Eos Trans. AGU*, 78(29), 293, 299–300, 1997.

Boucher, C., and Z. Altamimi, ITRF and its relationship to GPS, *GPS World Mag.*, 7, 71–74, 1996.

Carstensen, J. M., Description and simulation of visual texture, Ph.D. thesis, Inst. for Math. Model., Tech. Univ. of Denmark, Lyngby, 1992.

Carstensen, J. M., *Digital Image Processing*, Inst. for Math. Model., Tech. Univ. of Denmark, Lyngby, 1998.

Conzales, R. C., and R. E. Woods, *Digital Image Processing*, Addison-Wesley-Longman, Reading, Mass., 1993.

DeMets, C. G., R. G. Gordon, D. F. Argus, and S. Stein, Effect of recent revision to the geomagnetic reversal time scale on estimates of current plate motions, *Geophys. Res. Lett.*, 21, 2191–2194, 1994.

Einarsson, P., Earthquakes and present-day tectonism in Iceland, *Tectonophysics*, 189, 261–279, 1991.

Geman, S., and D. Geman, Stochastic relaxation, Gibbs distributions and the Bayesian restoration of images, *IEEE Trans. Pattern Anal. Mach. Intel.*, 6, 721–741, 1984.

Gudmundsson, S., Crustal deformation mapped by combined GPS and InSAR, M.Sc. thesis, Inst. for Math. Model., Tech. Univ. of Denmark, Lyngby, 2000. (Available at [http://www.norvol.hi.is/internal\\_rep.html](http://www.norvol.hi.is/internal_rep.html))

Gudmundsson, S., J. M. Carstensen, and F. Sigmundsson, Unwrapping ground displacement signals in satellite radar interferograms with aid of GPS data and MRF regularization, *IEEE Trans. Geosci. Remote Sens.*, 40, 1743–1754, 2002a.

Gudmundsson, S., M. T. Gudmundsson, H. Björnsson, F. Sigmundsson, H. Rott, and J. M. Carstensen, Three-dimensional glacier surface motion maps at the Gjalp eruption site, Iceland, inferred from combined InSAR and other ice displacement data, *Ann. Glaciol.*, 34, 315–322, 2002b.

Hreinsdóttir, S., GPS Geodetic Measurements on the Reykjanes Peninsula, SW Iceland: Crustal Deformation from 1993 to 1998, M.Sc. thesis, Univ. of Iceland, Reykjavik, 1999.

Hreinsdóttir, S., P. Einarsson, and F. Sigmundsson, Crustal deformation at the oblique spreading Reykjanes Peninsula, SW Iceland: GPS measurements from 1993 to 1998, *J. Geophys. Res.*, 106, 13,803–13,816, 2001.

Journel, A. G., *Fundamentals of Geostatistics in Five Lessons, Short Course Geol.*, vol. 8, AGU, Washington, D. C., 1989.

Leick, A., *GPS Satellite Surveying*, John Wiley, New York, 1990.

Li, S. Z., *Markov Random Field Modelling in Computer Vision*, Springer-Verlag, New York, 1995.

Nielsen, A. A., Geostatistik og analyse af spatielle data, report, Inst. for Math. Model., Tech. Univ. of Denmark, Lyngby, 1998. (Available at <http://www.imm.dtu.dk/~aa/note67,153.pdf>).

Massonnet, D., and K. L. Feigl, Discrimination of geophysical phenomena in satellite radar interferograms, *Geophys. Res. Lett.*, 22, 1537–1540, 1995.

Massonnet, D., and K. L. Feigl, Radar interferometry and its applications to changes in the Earth’s surface, *Rev. Geophys.*, 36, 441–500, 1998.

Ross, S. M., *Introduction to Probability and Statistics for Engineers and Scientists*, John Wiley, New York, 1987.

Rothacher, M., T. A. Springer, S. Sachaer, G. Beutler, D. Ineichen, U. Wild, A. Wiget, C. Boucher, S. Botton, and H. Seeger, 1997 Annual report-CODE analysis center of the IGS, in *1997 Technical Reports*, edited by I. Mueller, R. Neilan, and K. Gowey, pp. 73–87, IGS Cent. Bur., Jet Propul. Lab., Pasadena, Calif., 1998.

Vadon, H., and F. Sigmundsson, Crustal deformation from 1992 to 1995 at the Mid-Atlantic Ridge, southwest Iceland, mapped by satellite radar interferometry, *Science*, 275, 194–197, 1997.

Williams, S., Y. Bock, and P. Fang, Integrated satellite interferometry: Tropospheric noise, GPS estimates and implications for interferometric synthetic aperture radar products, *J. Geophys. Res.*, 103, 27,051–27,067, 1998.

Zebker, H. A., and J. Villasenor, Decorrelation in interferometric radar echoes, *IEEE Trans. Geosci. Remote Sens.*, 30, 950–959, 1992.

S. Gudmundsson, Science Institute, University of Iceland, Hofsvallagata 53, IS-107 Reykjavik, Iceland. (sg@raunvis.hi.is)  
 J. M. Carstensen, Institute for Mathematical Modeling, Technical University of Denmark, DK-2800 Lyngby, Denmark. (jmc@imm.dtu.dk)  
 F. Sigmundsson, Nordic Volcanological Institute, Grensasvegur 50, IS-108 Reykjavik, Iceland. (fs@norvol.hi.is)